Exceptional entanglement phenomena: non-Hermiticity meeting non-classicality

Pei-Rong Han[1],* Fan Wu[1],* Xin-Jie Huang[1],* Huai-Zhi Wu[1], Chang-Ling Zou[2,3,8], Wei Yi[2,3,8], Mengzhen Zhang[4], Hekang Li[5], Kai Xu[5,6,8], Dongning Zheng[5,6,8], Heng Fan[5,6,8], Jianming Wen[7],† Zhen-Biao Yang[1,8],‡ and Shi-Biao Zheng[1,8]§

[1] *Fujian Key Laboratory of Quantum Information and Quantum Optics, College of Physics and Information Engineering, Fuzhou University, Fuzhou, Fujian, 350108, China*

[2] *CAS Key Laboratory of Quantum Information, University of Science and Technology of China, Hefei 230026, China*

[3] *CAS Center for Excellence in Quantum Information and Quantum Physics, University of Science and Technology of China, Hefei 230026, China*

[4] *Pritzker School of Molecular Engineering, University of Chicago, Chicago, IL 60637, USA*

[5] *Institute of Physics, Chinese Academy of Sciences, Beijing 100190, China*

[6] *CAS Center for Excellence in Topological Quantum Computation, University of Chinese Academy of Sciences, Beijing 100190, China*

[7] *Department of Physics, Kennesaw State University, Marietta, Georgia 30060, USA*

[8] *Hefei National Laboratory, Hefei 230088, China*

Non-Hermitian (NH) extension of quantum-mechanical Hamiltonians represents one of the most significant advancements in physics. During the past two decades, numerous captivating NH phenomena have been revealed and demonstrated, but all of which can appear in both quantum and classical systems. This leads to the fundamental question: What NH signature presents a radical departure from classical physics? The solution of this problem is indispensable for exploring genuine NH quantum mechanics, but remains experimentally untouched upon so far. Here we resolve this basic issue by unveiling distinct exceptional entanglement phenomena, exemplified by an entanglement transition, occurring at the exceptional point (EP) of NH interacting quantum systems. We illustrate and demonstrate such purely quantum-mechanical NH effects with a naturally-dissipative light-matter system, engineered in a circuit quantum electrodynamics architecture. Our results lay the foundation for studies of genuinely quantum-mechanical NH physics, signified by EP-enabled entanglement behaviors.

When a physical system undergoes dissipation, the Hermiticity of its Hamiltonian dynamics is broken down. As any system inevitably interacts with its surrounding environment by exchanging particles or energy, non-Hermitian (NH) effects are ubiquitous in both classical and quantum physics. Such effects were once thought to be detrimental, and needed to be suppressed for observing physical phenomena of interest and for technological applications, until the discovery that NH effects could represent a complex extension of quantum mechanics [1–3]. Since then, increasing efforts have been devoted to the exploration of NH physics, leading to findings of many intriguing phenomena that are uniquely associated with NH systems. Most of these phenomena are closely related to the exceptional points (EPs), where both the eigenenergies and the eigenvectors of the NH Hamiltonian coalesce [4–6]. In addition to fundamental interest, such NH effects promise the realization of enhanced sensors [7–11].

Hitherto, there have been a plethora of experimental investigations on genuinely NH phenomena, ranging from real-to-complex spectral transition to NH topology [12–20], as well as on relevant applications [21–25], most of which were performed with classically interacting but non-entangled systems. The past few years have witnessed a number of demonstrations of similar NH phenomena in different quantum systems, ranging from photons [26–28] to atoms [29–31] and ions [32, 33], and from nitrogen-vacancy centers [34–36] to superconducting circuits [37–39]. However, these experiments have been confined to realizations of NH semiclassical models, where the degree of freedom either of the light or of the matter was treated classically in the effective NH Hamiltonian describing the light-matter interaction, and consequently, the observed NH effects bear no relation to quantum entanglement. Indeed, all the genuinely NH effects demonstrated so far can occur in both quantum and classical systems. This naturally leads to an imperative

issue: What feature can simultaneously manifest non-Hermiticity and non-classicality? Recently, there has been a significant focus on nonequilibrium quantum phase transitions in the entanglement dynamics of NH many-body systems [40–42], but the purely quantum-mechanical NH features associated with the Hamiltonian eigenstates have remained unexplored.

We here perform an in-depth investigation on this fundamental problem, finding that dissipative interacting quantum systems can display exceptional entanglement phenomena. In particular, we discover an EP-induced entanglement transition, which represents a purely quantum-mechanical NH signature, with neither Hermitian nor classical analogs. We illustrate our discovery with a dissipative qubit-photon system, whose NH quantum effects are manifested by the singular entanglement behaviors of the bipartite entangled eigenstates. We experimentally demonstrated these singular behaviors in a circuit, where a superconducting qubit is controllably coupled to a decaying resonator. The exceptional entanglement signatures, inherent in the qubit-photon static eigenstates, are mapped out by a density matrix post-casting method, which enables us to extract the weak nonclassical signal from the strong noise background. In addition to the quantum character, the demonstrated NH phenomena originate from naturally occurring dissipation, distinct from that induced by an artificially engineered reservoir [12–39]. Our results are universal for composite quantum systems immersed in pervasive Markovian reservoirs, endowing NH quantum mechanics with genuinely non-classical characters, which are absent in NH classical physics.

The theoretical model, used to illustrate the NH entanglement transition, is composed of a two-level system (qubit) resonantly coupled to a quantized photonic mode, as sketched in Fig. 1a. The quantum state evolution trajectory without photon-number jumps is governed by the NH Hamiltonian (setting $\hbar = 1$)

$$\mathcal{H}_{NH} = \Omega(a^\dagger |g\rangle \langle e| + a |e\rangle \langle g|) - \frac{i}{2}\kappa_q |e\rangle \langle e| - \frac{i}{2}\kappa_f a^\dagger a, \tag{1}$$

where $|e\rangle$ ($|g\rangle$) denotes the upper (lower) level of the qubit, $a^\dagger$ (a) represents the creation (annihilation) operator for the photonic mode, κ_q (κ_f) is the energy dissipation rate for the qubit (field mode), and Ω is the qubit-field coupling strength. In the n-excitation subspace, the system has two right entangled eigenstates, given by

$$|\Phi_{n,\pm}\rangle = \mathcal{N}_{n,\pm}(\sqrt{n}\Omega |e, n-1\rangle + E_{n,\pm} |g, n\rangle), \tag{2}$$

where $\mathcal{N}_{n,\pm} = (n\Omega^2 + |E_{n,\pm}|^2)^{-1/2}$ and $E_{n,\pm} = -i\gamma/4 \pm \Delta E_n/2$ are the corresponding eigenenergies, with $\gamma = \kappa_f + \kappa_q$, $\Delta E_n = 2\sqrt{n\Omega^2 - \kappa^2/16}$, and $\kappa = \kappa_f - \kappa_q$. These two eigenstates are separated by an energy gap of ΔE_n. The inherent quantum entanglement makes the system fundamentally distinct from previously demonstrated NH semiclassical models [29–39], where the qubit is not entangled with the classical control field in any way. When $\Omega > \kappa/(4\sqrt{n})$, the system has a real energy gap, and undergoes Rabi-like oscillations, during which the qubit periodically exchanges a photon with the field mode. With the decrease of Ω, the energy gap is continuously narrowed until reaching the EP, where the two energy levels coalesce. After crossing the EP, the gap becomes imaginary, and the population evolution exhibits an over-damping feature.

Unlike previous investigations, here each eigenenergy is possessed by the two entangled components, neither of which has its own state. The nonclassical feature of each eigenstate is manifested by the light-matter entanglement, which can be quantified by the concurrence [43]

$$\mathcal{E}_\pm = \frac{2\sqrt{n}\Omega |E_{n,\pm}|}{|E_{n,\pm}|^2 + n\Omega^2}. \tag{3}$$

When the rescaled coupling strength $\eta = 4\sqrt{n}\Omega/\kappa$ is much smaller than 1, the two eigenstates are respectively dominated by $|e, n-1\rangle$ and $|g, n\rangle$. With the increase of η, these two populations become increasingly balanced until reaching the EP $\eta = 1$, where both eigenstates converge to the same maximally entangled state. During this convergence, $\mathcal{E}_\pm$ exhibit a linear scaling with η. In the Bloch representation, this corresponds to a rotation of the eigenvector $|\Phi_{n,+}\rangle$ ($|\Phi_{n,-}\rangle$) around the x ($-x$) axis from pointing at the north (south) polar, until merging at the y axis, as shown in the left panel of Fig. 1b. After crossing the EP, $\mathcal{E}_\pm$ become independent of Ω, which implies both two eigenstates keep maximally entangled. However, $|\Phi_{n,+}\rangle$ ($|\Phi_{n,-}\rangle$) is rotated around the z ($-z$) axis, progressively approaching the x ($-x$) axis (right panel of Fig. 1b). This sudden switch of the rotation axis manifests an entanglement transition at the EP, where the derivative of the concurrence with respect to η presents a discontinuity, jumping from 1 to 0. By measuring the time-evolving output states associated with the no-jump trajectory, we can extract the information about both the energy gap and entanglement regarding the "static" eigenstates. It should be noted that the resonator plays a radically different role from the ancilla used in the previous experiments [34–37], which was

introduced as an artificially engineered environment to the test qubit, but whose dynamics was not included in the effective NH Hamiltonian dynamics. In distinct contrast, in the present system the degree of freedom of R constitutes a part of the Hamiltonian, whose NH term is induced by the natural environment.

The experimental demonstration of the NH physics is performed in a circuit quantum electrodynamics architecture, where the qubit-photon model is realized with a superconducting qubit Q and its resonator R with a fixed frequency $\omega_r/2\pi = 6.66$ GHz (see Supplemental Material, Sec. S2 [45]). The decaying rates of Q and R are $\kappa_q \simeq 0.07$ MHz and $\kappa_f = 5$ MHz, respectively. The accessible maximum frequency of Q, $\omega_{\max} = 2\pi \times 6.01$ GHz, is lower than ω_r by an amount much larger than their on-resonance swapping coupling $g_r = 2\pi \times 41$ MHz (Fig. 1c). To observe the EP physics, an ac flux is applied to Q, modulating its frequency as $\omega_q = \omega_0 + \varepsilon\cos(\nu t)$, where ω_0 is the mean $|e\rangle$-$|g\rangle$ energy difference, and ε and ν denote the modulating amplitude and frequency. This modulation enables Q to interact with R at a preset sideband, with the photon swapping rate Ω tunable by ε (see Supplemental Material, Sec. S3 [45]).

Our experiment focuses on the single-excitation case ($n = 1$). Before the experiment, the system is initialized to the ground state $|g, 0\rangle$. The experiment starts by transforming Q from the ground state $|g\rangle$ to excited state $|e\rangle$ with a π pulse, following which the parametric modulation is applied to Q to initiate the Q-R interaction (see Fig. S4 of Supplementary Material for the pulse sequence). This interaction, together with the natural dissipations, realizes the NH Hamiltonian of Eq. (1). After the modulating pulse, the Q-R state is measured with the assistance of an ancilla qubit (Q_a) and a bus resonator (R_b), which is coupled to both Q and Q_a. The subsequent $Q \to R_b$, $R_b \to Q_a$, and $R \to Q$ quantum state transferring operations map the Q-R output state to the Q_a-Q system, whose state can be read out by quantum state tomography (see Supplemental Material, Sec. S5 [45]).

A defining feature of our system is the conservation of the excitation number under the NH Hamiltonian. This Hamiltonian evolves the system within the subspace $\{|e, 0\rangle, |g, 1\rangle\}$. A quantum jump would disrupt this conversion, moving the system out of this subspace. This property in turn enables us to post-select the output state governed the NH Hamiltonian simply by discarding the joint Q_a-Q outcome $|g, g\rangle$ after the state mapping. With a correction of the quantum state distortion caused by the decoherence occurring during the state mapping, we can infer the quantum Rabi oscillatory signal, characterized by the evolution of the joint probability $|e, 0\rangle$, denoted as $P_{e,0}$. Fig. 2a shows thus-obtained $P_{e,0}$ as a function of the rescaled coupling η and the Q-R interaction time t. The results clearly show that both the shapes and periods of vacuum Rabi oscillations are significantly modulated by the NH term around the EP $\eta = 1$, where incoherent dissipation is comparable to the coherent interaction. These experimental results are in well agreement with numerical simulations (see Supplemental Material, Sec. S4 [45]).

The Rabi signal does not unambiguously reveal the system's quantum behavior. To extract full information of the two-qubit entangled state, it is necessary to individually measure all three Bloch vectors for each qubit, and then correlate the results for the two qubits. The z-component can be directly measured by state readout, while measurements of the x- and y-components require y-rotations and x-rotations before state readout, which breaks down excitation-number conservation, and renders it impossible to distinguish individual jump events from no-jump ones. We circumvent this problem by first reconstructing the two-qubit density matrix using all the measurement outcomes, and then discarding the matrix elements associated with $|g, g\rangle$ (see Supplemental Material, Sec. S5 [45]). This effectively post-casts the two-qubit state to the subspace $\{|e, g\rangle, |g, e\rangle\}$. We note that such a technique is in sharp contrast with the conventional post-selection method, where some auxiliary degree of freedom (e.g., propagation direction of a photon) enables reconstruction of the relevant conditional output state, but which is unavailable in the NH qubit-photon system. With a proper correction for the state mapping error, we obtain the Q-R output state governed by the non-Hermitian Hamiltonian. In Fig. 2b, we present the resulting Q-R concurrence, as a function of η and t. To show the entanglement behaviors more clearly, we present the concurrence evolutions for $\eta = 5$ and 0.5 in Fig. 2c and d, respectively. The results demonstrate that the entanglement exhibits distinct evolution patterns in the regimes above and below the EP.

To reveal the close relation between the exceptional entanglement behavior and the EP, we infer the eigenvalues and eigenstates of the NH Hamiltonian from the output states, measured for different evolution times (see Supplemental Material, Sec. S7 [45]). The concurrences associated with the two eigenstates, obtained for different values of η, are shown in Fig. 3a and b (dots), respectively. As expected, each of these entanglements exhibits a linear scaling below the EP, but is saturated at the EP, and no longer depends upon η after crossing the EP. The singular features around the EP are manifested by their derivatives to η, which are shown in the insets. The discontinuity of these derivatives indicates the occurrence of an entanglement transition at the EP. Such a nonclassical behavior, as a consequence of the competition between the coherent coupling and incoherent dissipation, represents a unique character of strongly correlated NH quantum systems, but has not been reported so far. These results demonstrate a longitudinal merging of the two entangled eigenstates at the EP (left panel of Fig. 2b). Accompanying this is the onset of the transverse splitting, which can be characterized by the relative phase difference between $|\Phi_{1,\pm}\rangle$, defined as $\varphi = \varphi_+ - \varphi_-$, with $\varphi_\pm$ representing the relative phases between $|g, 1\rangle$ and $|e, 0\rangle$ in the eigenstates $|\Phi_{1,\pm}\rangle$. Such a phase difference, inferred

for different values of η, is displayed in Fig. 3c. This quantum-mechanical NH signature is universally applicable to dissipative interacting quantum systems, a feature absent in earlier superconducting-circuit-based single-qubit NH experiments [38, 39].

The demonstrated exceptional entanglement transition is a purely quantum-mechanical NH effect. On one hand, quantum entanglement, which has no classical analogs, represents a most characteristic trait that distinguishes quantum physics from classical mechanics [46]. On the other hand, this effect, uniquely associated with the EP, is absent in Hermitian qubit-photon systems [47–50]. We further note that such an NH effect can occur in other dissipative quantum-mechanically correlated systems, e.g., a system composed of two or more coupled qubits with unbalanced decaying rates (see Supplemental Material, Sec. S8 [45]). This implies that such a quantum-mechanical NH signature is universal for dissipative interacting quantum systems.

The real and imaginary parts of the extracted quantum Rabi splitting ΔE_n are shown in Fig. 3d. As theoretically predicted, above the EP the two eigenenergies have a real gap, which is continuously narrowed when the control parameter η is decreased until reaching the EP, where the two levels coalesce. After crossing the EP, the two levels are re-split but with an imaginary gap, which increases when η is decreased. This corresponds to the real-to-imaginary transition of the vacuum Rabi splitting between the Q-R entangled eigenstates, which is in distinct contrast with the previous experiments on $\mathcal{PT}$ symmetry breaking [29–39], realized with the semiclassical models, where the exceptional physics has no relation with quantum entanglement.

In conclusion, we have discovered an exceptional entanglement transition in a fundamental light-matter system governed by an NH Hamiltonian, establishing a close connection between quantum correlations and non-Hermitian effects. This transition has neither Hermitian nor classical analogs, representing the unique feature of NH quantum mechanics. The experimental demonstration is performed in a circuit, where a superconducting qubit is controllably coupled to a resonator with a non-negligible dissipation induced by a natural Markovian reservoir. The NH quantum signatures of the eigenstates are inferred from the no-jump output state, measured for different evolution times. Our results push NH Hamiltonian physics from the classical to genuinely non-classical regime, where the emergent phenomena have neither Hermitian nor classical analogs. The post-projection method, developed for extracting the no-jump output density matrix, would open the door to experimentally explore purely quantum-mechanical NH effects in a broad spectrum of interacting systems, where excitation number is initially definite and conserved under the NH Hamiltonian. Such systems include resonator-qubits arrays [51], fully-connected architectures involving multiple qubits coupled to a single resonator [52], and lattices composed of many qubits with nearest-neighbor coupling [53]. When the system initially has n excitations, the no-jump trajectory can be post-selected by discarding the outcomes with less than n excitations.

Acknowledgments: We thank Liang Jiang at University of Chicago for valuable comments. Funding: This work was supported by the National Natural Science Foundation of China (Grant No. 12274080, No. 11875108, No. 12204105, No. 11774058, No. 12174058, No. 11974331, No. 11934018, No. 92065114, and No. T2121001), Innovation Program for Quantum Science and Technology (Grant No. 2021ZD0300200 and No. 2021ZD0301200), NSF (Grant No. 2329027), the Strategic Priority Research Program of Chinese Academy of Sciences (Grant No. XDB28000000), the National Key R&D Program under (Grant No. 2017YFA0304100), the Key-Area Research and Development Program of Guangdong Province, China (Gran No. 2020B0303030001), Beijing Natural Science Foundation (Grant No. Z200009), and the Project from Fuzhou University (Grant No. 049050011050).

Author contributions: S.B.Z. predicted the exceptional entanglement transition and conceived the experiment. P.R.H. and X.J.H., supervised by Z.B.Y. and S.B.Z., carried out the experiment. F.W., P.R.H., J.W., and S.B.Z. analyzed the data. S.B.Z., J.W., Z.B.Y., and W.Y. cowrote the paper. All authors contributed to interpretation of observed phenomena and helped to improve presentation of the paper.

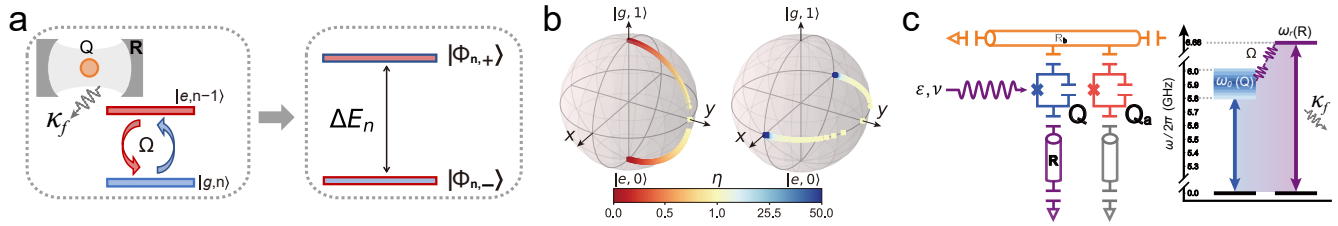

FIG. 1: **NH Light-matter interaction and experimental implementation.** (a) Theoretical model. The system under investigation involves a quantized field mode with a decaying rate κ_f resonantly interacting with a matter qubit with a decaying rate κ_q. Their interaction is characterized by a coupling strength of Ω. The system's dynamics can be cast onto different U(1)-symmetric eigenspaces, denoted as $\{|e,n-1\rangle, |g,n\rangle\}$, within each of which there exist two eigenstates $|\Phi_{n,\pm}\rangle$, separated by a gap of ΔE_n. (b) Bloch representation of $|\Phi_{1,\pm}\rangle$ in the single-excitation subspace ($n=1$). For clarity, we here pictorially display the dependence of $|\Phi_{1,\pm}\rangle$ on the rescaled coupling strength $\eta = 4\Omega/\kappa$. For $\eta = 0$, $|\Phi_{1,\pm}\rangle$ correspond to $|e,0\rangle$ and $|g,1\rangle$, respectively. With the increase of η, $|\Phi_{1,\pm}\rangle$ are respectively rotated around $\pm x$ axes, and merged to the y axis at the EP $\eta = 1$, featuring the occurrence of the maximally entangled state $|Y\rangle = (|g,1\rangle - i\,|e,0\rangle)/\sqrt{2}$. After crossing the EP, the eigenvectors $|\Phi_{1,\pm}\rangle$ remain on the equatorial plane, but are rotated around the z and $-z$ axes, progressively aligned with the $\pm x$ axes, tending to $|\pm X\rangle = (|g,1\rangle \pm |e,0\rangle)/\sqrt{2}$, respectively. (c) Implementation of the NH Hamiltonian. In the experimental system, a superconducting qubit Q is highly detuned from the lossy resonator R with a fixed frequency $\omega_r/2\pi = 6.66$ GHz. The Q-R interaction is enabled with an ac flux, which modulates Q's energy gap around the mean value ω_0, with a frequency ν, mediating a photonic swapping coupling at one sideband, with the coupling strength controlled by the modulating amplitude ε.

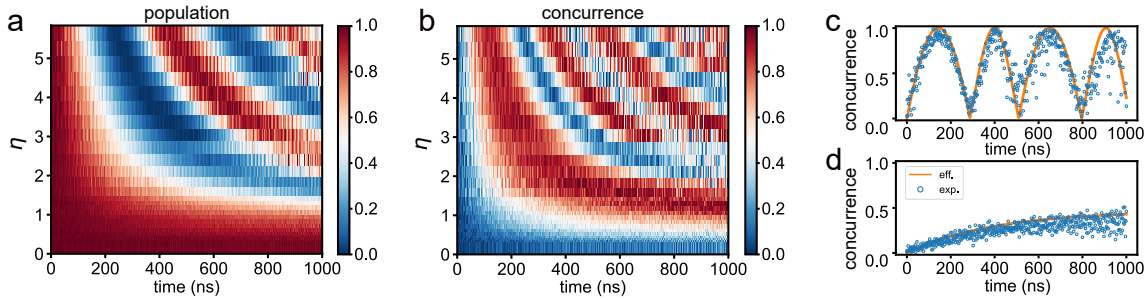

FIG. 2: **Characterization of NH dynamical evolutions.** (a) Measured evolutions of the population $|e,0\rangle$ for different values of the rescaled coupling η. The signals are extracted by correlating the measurement outcomes of Q and Q_a, which correspond to the outputs of R and Q right before the state mappings. The NH Hamiltonian evolution trajectory is post-selected by discarding the detection events $|g,g\rangle$, and renormalizing the remaining outcomes $|g,e\rangle$ and $|e,g\rangle$. (b) Evolutions of the concurrences for different values of η. The concurrence at each point is inferred with the post-projected density matrix, obtained by reconstructing the output Q-Q_a density matrix, projecting the thus-obtained two-qubit state to the reduced subspace with one excitation, and then renormalizing the remaining matrix elements. (c), (d) Concurrence evolutions for $\eta = 5$ (c) and 0.5 (d). The orange solid curves are the numerical simulations using the effective Hamiltonian and the blue circles are the experimental results.

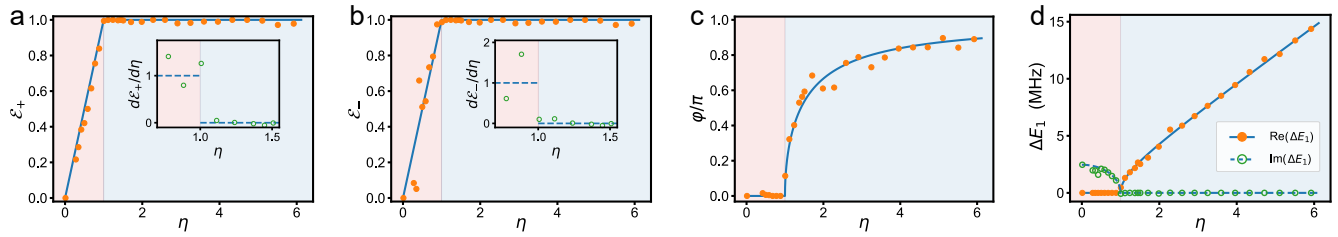

FIG. 3: **Observation of exceptional phase transitions.** (a), (b) Entanglements for the eigenstates $|\Phi_{1,+}\rangle$ and $|\Phi_{1,-}\rangle$ versus η. We obtain the concurrences $\mathcal{E}_\pm$ at each point based on the corresponding eigenstates, which are mapped out from the Q-R output states, measured for different evolution times. The dots denote the inferred concurrences, which well agree with the results for the ideal output states. The derivatives $d\mathcal{E}_\pm/d\eta$ around the EP, obtained by $[\mathcal{E}_\pm(\eta+\delta\eta) - \mathcal{E}_\pm(\eta)]/\delta\eta$, is displayed in the insets. (c) Relative phase difference (φ) between $|\Phi_{1,\pm}\rangle$. This phase difference is defined as $\varphi = \varphi_+ - \varphi_-$, where $\varphi_\pm$ are the relative phase between $|g,1\rangle$ and $|e,0\rangle$ in the eigenstates $|\Phi_{1,\pm}\rangle$. (d) Spectral gap ΔE_1. As the eigenspectrum is possessed by the entangled eigenstates of the Q-R system, this gap corresponds to the vacuum Rabi splitting. The solid and dashed lines denote the real and imaginary parts, respectively.

* These authors contribute equally to this work.
† E-mail: jianming.wen@gmail.com
‡ E-mail: zbyang@fzu.edu.cn
§ E-mail: t96034@fzu.edu.cn

[1] C. M. Bender and S. Boettcher, Real spectra in non-Hermitian Hamiltonians having $\mathscr{P}\mathscr{T}$ symmetry, *Phys. Rev. Lett.* **80,** 5243 (1998).
[2] C. M. Bender, D. C. Brody, and H. F. Jones, Complex extension of quantum mechanics, *Phys. Rev. Lett.* **89,** 270401 (2002).
[3] N. Moiseyev, *Non-Hermitian Quantum Mechanics* (Cambridge Univ. Press, 2011).
[4] Ş. K. Özdemir, S. Rotter, F. Nori, and L. Yang, Parity–time symmetry and exceptional points in photonics, *Nat. Mater.* **18,** 783-798 (2019).
[5] E. J. Bergholtz, J. C. Budich, and F. K. Kunst, Exceptional topology of non-Hermitian systems, *Rev. Mod. Phys.* **93,** 015005 (2021).
[6] K. Ding, C. Fang, and G. Ma, Non-Hermitian topology and exceptional-point geometries, *Nat. Rev. Phys.* **4,** 745–760 (2022).
[7] Z.-P. Liu, J. Zhang, Ş. K. Özdemir, B. Peng, H. Jing, X.-Y. Lü, C.-W. Li, L. Yang, F. Nori, and Y.-X Liu, Metrology with $\mathcal{PT}$-symmetric cavities: enhanced sensitivity near the $\mathcal{PT}$-phase transition, *Phys. Rev. Lett.* **117,** 110802 (2016).
[8] M. Zhang, W. Sweeney, C. W. Hsu, L. Yang, A. D. Stone, and L. Jiang, Quantum noise theory of exceptional point amplifying sensors, *Phys. Rev. Lett.* **123,** 180501 (2019).
[9] Y. Chu, Y. Liu, H. Liu, and J. Cai, Quantum sensing with a single-qubit pseudo-Hermitian system, *Phys. Rev. Lett.* **124,** 020501 (2020).
[10] X.-W Luo, C. Zhang, and S. Du, Quantum squeezing and sensing with pseudo anti-parity-time symmetry, *Phys. Rev. Lett.* **128,** 173602 (2022).
[11] J. Wang, D. Mukhopadhyay, and G. S. Agarwal, Quantum Fisher information perspective on sensing in anti-PT symmetric systems, *Phys. Rev. Res.* **4,** 013131 (2022).
[12] C. Dembowski, H.-D. Gräf, H. L. Harney, A. Heine, W. D. Heiss, H. Rehfeld, and A. Richter, Experimental observation of the topological structure of exceptional points, *Phys. Rev. Lett.* **86,** 787 (2001).
[13] Y. Choi, S. Kang, S. Lim, W. Kim, J.-R. Kim, J.-H. Lee, and K. An, Quasieigenstate coalescence in an atom-cavity quantum composite, *Phys. Rev. Lett.* **104,** 153601 (2010).
[14] T. Gao *et al.*, Observation of non-Hermitian degeneracies in a chaotic exciton-polariton billiard, *Nature* **526,** 554-558 (2015).
[15] D. Zhang, X.-Q. Luo, Y.-P. Wang, T.-F. Li, and J. Q. You, Observation of the exceptional point in cavity magnon-polaritons, *Nat. Commun.* **8,** 1368 (2017).
[16] F. E. Öztürk, T. Lappe, G. Hellmann, J. Schmitt, J. Klaers, and F. Vewinger, Observation of a non-Hermitian phase transition in an optical quantum gas, *Science* **372,** 88-91 (2021).
[17] W. Tang, X. Jiang, K. Ding, Y.-X. Xiao, Z.-Q. Zhang, C. T. Chan, and G. Ma, Exceptional nexus with a hybrid topological invariant, *Science* **370,** 1077-1080 (2020).
[18] K. Wang, A. Dutt, K. Y. Yang, C. C. Wojcik, J. Vučković, and S. Fan, Generating arbitrary topological windings of a non-Hermitian band, *Science* **371,** 1240-1245 (2021).
[19] K. Wang, A. Dutt, C. C. Wojcik, and S. Fan, Topological complex-energy braiding of non-Hermitian bands, *Nature* **598,** 59-64 (2021).
[20] Y. S. S. Patil, J. Höller, P. A. Henry, C. Guria, Y. Zhang, L. Jiang, N. Kralj, N. Read, and J. G. E. Harris, Measuring the knot of non-Hermitian degeneracies and non-commuting braids, *Nature* **607,** 271-275 (2022).
[21] J. Doppler, A. A. Mailybaev, J. Böhm, U. Kuhl, A. Girschik, F. Libisch, T. J. Milburn, P. Rabl, N. Moiseyev, and S. Rotter, Dynamically encircling an exceptional point for asymmetric mode switching, *Nature* **537,** 76-79 (2016).
[22] H. Xu, D. Mason, L. Jiang, and J. G. E. Harris, Topological energy transfer in an optomechanical system with exceptional points, *Nature* **537,** 80-83 (2016).
[23] J. W. Yoon *et al.*, Time-asymmetric loop around an exceptional point over the full optical communication band, *Nature* **562,** 86-90 (2018).
[24] W. Chen, Ş. K. Özdemir, G. Zhao, J. Wiersig, and L. Yang, Exceptional points enhance sensing in an optical microcavity, *Nature* **548,** 192-196 (2017).
[25] H. Hodaei, A. U. Hassan, S. Wittek, H. Garcia-Gracia, R. El-Ganainy, D. N. Christodoulides, and M. Khajavikhan, Enhanced sensitivity at higher-order exceptional points, *Nature* **548,** 187-191 (2017).
[26] S. Yu *et al.*, Experimental investigation of quantum $\mathcal{PT}$-enhanced sensor, *Phys. Rev. Lett.* **125,** 240506 (2020).
[27] K. Wang, L. Xiao, J. C. Budich, W. Yi, and P. Xue, Simulating exceptional non-Hermitian metals with single-photon interferometry, *Phys. Rev. Lett.* **127,** 026404 (2021).
[28] Y.-L. Fang, J.-L. Zhao, Y. Zhang, D.-X. Chen, Q.-C. Wu, Y.-H. Zhou, C.-P. Yang, and F. Nori, Experimental demonstration of coherence flow in PT- and anti-PT-symmetric systems, *Commun. Phys.* **4,** 223 (2021).
[29] P. Peng, W. Cao, C. Shen, W. Qu, J. Wen, L. Jiang, and Y. Xiao, Anti-parity-time symmetry with flying atoms, *Nat. Phys.* **12,** 1139-1145 (2016).

[30] J. Li, A. K. Harter, J. Liu, L. d. Melo, Y. N. Joglekar, and L. Luo, Observation of parity-time symmetry breaking transitions in a dissipative Floquet system of ultracold atoms, *Nat. Commun.* **10,** 855 (2019).

[31] Z. Ren, D. Liu, E. Zhao, C. He, K. K. Pak, J. Li, and G.-B. Jo, Chiral control of quantum states in non-Hermitian spin-orbit-coupled fermions, *Nat. Phys.* **18,** 385-389 (2022).

[32] W.-C. Wang *et al.*, Observation of $\mathcal{PT}$-symmetric quantum coherence in a single-ion system, *Phys. Rev. A* **103,** L020201 (2021).

[33] L. Ding, K. Shi, Q. Zhang, D. Shen, X. Zhang, and W. Zhang, Experimental determination of $\mathcal{PT}$-symmetric exceptional points in a single trapped ion, *Phys. Rev. Lett.* **126,** 083604 (2021).

[34] Y. Wu, W. Liu, J. Geng, X. Song, X. Ye, C. K. Duan, X. Rong, and J. F. Du, Observation of parity-time symmetry breaking in a single-spin system, *Science* **364,** 878–880 (2019).

[35] W. Liu, Y. Wu, C.-K. Duan, X. Rong, and J. Du, Dynamically encircling an exceptional point in a real quantum system, *Phys. Rev. Lett.* **126,** 170506 (2021).

[36] W. Zhang, X. Ouyang, X. Huang, X. Wang, H. Zhang, Y. Yu, X. Chang, Y. Liu, D.-L. Deng, and L.-M. Duan, Observation of non-Hermitian topology with nonunitary dynamics of solid-state spins, *Phys. Rev. Lett.* **127,** 090501 (2021).

[37] S. Dogra, A. A. Melnikov, and G. S. Paraoanu, Quantum simulation of parity-time symmetry breaking with a superconducting quantum processor, *Commun. Phys.* **4,** 26 (2021).

[38] M. Naghiloo, M. Abbasi, Y. N. Joglekar, and K. W. Murch, Quantum state tomography across the exceptional point in a single dissipative qubit, *Nat. Phys.* **15,** 1232-1236 (2019).

[39] Z. Wang, Z. Xiang, T. Liu, X. Song, P. Song, X. Guo, L. Su, H. Zhang, Y. Du, and D. Zheng, Observation of the exceptional point in superconducting qubit with dissipation controlled by parametric modulation, *Chin. Phys. B* **30,** 100309 (2021).

[40] K. Kawabata, T. Numasawa, and S. Ryu, Entanglement Phase Transition Induced by the Non-Hermitian Skin Effect, *Phys. Rev. X* **13,** 021007 (2023).

[41] X. Turkeshi and M. Schiró, Entanglement and correlation spreading in non-Hermitian spin chains, *Phys. Rev. B* **107,** L020403 (2023).

[42] Y. L. Gal, X. Turkeshi, and M. Schiró, Volume-to-area law entanglement transition in a non-Hermitian free fermionic chain, *SciPost Phys.* **14,** 138 (2023).

[43] W. K. Wootters, Entanglement of formation of an arbitrary state of two qubits, *Phys. Rev. Lett.* **80,** 2245 (1998).

[44] R. Horodecki, P. Horodecki, M. Horodecki, and K. Horodecki, Quantum entanglement, *Rev. Mod. Phys.* **81,** 865 (2009).

[45] See Supplemental Material for detailed calculations of the concurrences and negativities for the eigenstates and NH-Hamiltonian-evolved states, a description of system parameters, a derivation of the effective Q-R interaction Hamiltonian, numerical simulations of the NH Hamiltonian dynamics, discussions of measurement of the Q-R output state and of extraction of the NH Hamiltonian eigenenergies and eigenstates, as well as an investigations on the exceptional entanglement transition in a two-qubit system, which includes Refs. [43, 44, 54-57].

[46] V. Vedral, Quantum entanglement, *Nat. Phys.* **10,** 256–258 (2014).

[47] R. J. Thompson, G. Rempe, and H. J. Kimble, Observation of normal-mode splitting for an atom in an optical cavity, *Phys. Rev. Lett.* **68,** 1132 (1992).

[48] F. Bernardot, P. Nussenzveig, M. Brune, J. M. Raimond, and S. Haroche, Vacuum Rabi splitting observed on a microscopic atomic sample in a microwave cavity, *Europhys. Lett.* **17,** 33 (1992).

[49] J. M. Fink, M. Goppl, M. Baur, R. Bianchetti, P. J. Leek, A. Blais, and A. Wallraff, Climbing the Jaynes-Cummings ladder and observing its nonlinearity in a cavity QED system, *Nature* **454,** 315-318 (2008).

[50] L. S. Bishop, J. M. Chow, J. Koch, A. A. Houck, M. H. Devoret, E. Thuneberg, S. M. Girvin, and R. J. Schoelkopf, Nonlinear response of the vacuum Rabi resonance, *Nat. Phys.* **5,** 105-109 (2009).

[51] M. Mariantoni *et al.*, Photon shell game in three-resonator circuit quantum electrodynamics, *Nat. Phys.* **7,** 287-293 (2011).

[52] C. Song *et al.*, Generation of multicomponent atomic Schrödinger cat states of up to 20 qubits, *Science* **365,** 574 (2019).

[53] M. Gong *et al.*, Quantum walks on a programmable two-dimensional 62-qubit superconducting processor, *Science* **372,** 948 (2021).

[54] S.-B. Zheng and G.-C. Guo, Efficient scheme for two-atom entanglement and quantum information processing in cavity QED, *Phys. Rev. Lett.* **85,** 2392 (2000).

[55] S. Osnaghi, P. Bertet, A. Auffeves, P. Maioli, M. Brune, J. M. Raimond, and S. Haroche, Coherent control of an atomic collision in a cavity, *Phys. Rev. Lett.* **87,** 037902 (2001).

[56] C. Song, K. Xu, W. Liu, C.-P. Yang, S.-B. Zheng, H. Deng *et al.*, 10-qubit entanglement and parallel logic operations with a superconducting circuit, *Phys. Rev. Lett.* **119,** 180511 (2017).

[57] Y. Zhou *et al.*, Rapid and unconditional parametric reset protocol for tunable superconducting qubits, *Nat. Commun.* **12,** 5924 (2021).

Supplementary Materials for "Exceptional entanglement phenomena: non-Hermiticity meeting non-classicality"

Pei-Rong Han[1],* Fan Wu[1],* Xin-Jie Huang[1],* Huai-Zhi Wu[1], Chang-Ling Zou[2,3,8], Wei Yi[2,3,8], Mengzhen Zhang[4], Hekang Li[5], Kai Xu[5,6,8], Dongning Zheng[5,6,8], Heng Fan[5,6,8], Jianming Wen[7],† Zhen-Biao Yang[1,8],‡ and Shi-Biao Zheng[1,8]§

[1] *Fujian Key Laboratory of Quantum Information and Quantum Optics, College of Physics and Information Engineering, Fuzhou University, Fuzhou, Fujian, 350108, China*

[2] *CAS Key Laboratory of Quantum Information, University of Science and Technology of China, Hefei 230026, China*

[3] *CAS Center for Excellence in Quantum Information and Quantum Physics, University of Science and Technology of China, Hefei 230026, China*

[4] *Pritzker School of Molecular Engineering, University of Chicago, Chicago, IL 60637, USA*

[5] *Institute of Physics, Chinese Academy of Sciences, Beijing 100190, China*

[6] *CAS Center for Excellence in Topological Quantum Computation, University of Chinese Academy of Sciences, Beijing 100190, China*

[7] *Department of Physics, Kennesaw State University, Marietta, Georgia 30060, USA*

[8] *Hefei National Laboratory, Hefei 230088, China*

Contents

*These authors contribute equally to this work.
†E-mail: jianming.wen@kennesaw.edu
‡E-mail: zbyang@fzu.edu.cn
§E-mail: t96034@fzu.edu.cn

S1 . ENTANGLEMENT OF THE EIGENSTATES AND NH-HAMILTONIAN-EVOLVED STATE

When the qubit-resonator system is restricted in the n-excitation subspace, the resonator can be thought of as a qubit with two basis vectors $|n-1\rangle$ and $|n\rangle$. With this analogy, the qubit-resonator model corresponds to a composite system composed of two qubits, whose entanglement can be quantified in terms of the eigenvalues of the operator [5]

$$\widetilde{\rho} = \rho(\sigma_y^q \otimes \sigma_y^r)\rho^*(\sigma_y^q \otimes \sigma_y^r), \tag{S1}$$

where ρ is the density operator of the composite system, and σ_y^q and σ_y^r denote the corresponding y-component Pauli operators of the two qubits, defined as

$$\sigma_y^q = -i\,|g\rangle\langle e| + i\,|e\rangle\langle g|\,, \tag{S2}$$
$$\sigma_y^r = -i\,|n-1\rangle\langle n| + i\,|n\rangle\langle n-1|\,. \tag{S3}$$

Suppose that $\lambda_1 \geq \lambda_2 \geq \lambda_3 \geq \lambda_4$ are the square roots of the eigenvalues of $\widetilde{\rho}$. Then the two-qubit entanglement associated with the density matrix ρ is measured by the quantity

$$\mathcal{E} = \max\{\lambda_1 - \lambda_2 - \lambda_3 - \lambda_4,\, 0\}. \tag{S4}$$

$\mathcal{E}$ is referred to as concurrence [5], ranging from 0 to 1.

For the eigenstates $|\Phi_{n,\pm}\rangle$ of the NH Hamiltonian, given by Eq. (2) of the main text, the system density operator in the basis $\{|g,n-1\rangle, |g,n\rangle, |e,n-1\rangle, |e,n\rangle\}$ can be expressed as

$$\rho_{n,\pm} = |\mathcal{N}_{n,\pm}|^2 \begin{pmatrix} 0 & 0 & 0 & 0 \\ 0 & |E_{n,\pm}|^2 & \sqrt{n}\Omega E_{n,\pm} & 0 \\ 0 & \sqrt{n}\Omega E_{n,\pm}^* & n\Omega^2 & 0 \\ 0 & 0 & 0 & 0 \end{pmatrix}. \tag{S5}$$

The corresponding matrix $\widetilde{\rho}$ has a single non-zero eigenvalue, given by $4n\,|\Omega E_{n,\pm}|^2\,\mathcal{N}_{n,\pm}^4$. The resulting concurrence is

$$\mathcal{E}_\pm = 2\sqrt{n}\Omega\,|E_{n,\pm}|\,\mathcal{N}_{n,\pm}^2 \tag{S6}$$
$$= \frac{2\sqrt{n}\Omega\,|E_{n,\pm}|}{|E_{n,\pm}|^2 + n\Omega^2}. \tag{S7}$$

When $\eta = 4\Omega/\kappa < 1$, the concurrence of each eigenstate increases linearly with η until reaching the maximum 1 at the EP. After crossing the EP, the concurrence becomes independent of η. This exceptional entanglement transition can be elucidated as follows. The entanglement between the qubit and the photonic mode arises from the coherent superposition of the two basis vectors $|e,n-1\rangle$ and $|g,n\rangle$. The amount of entanglement hinges on the relative weighting of these basis vectors. Below the EP, their populations are unequal in each eigenstate. As η increases, these populations gradually balance until $\eta = 1$. Beyond this point, further increments in η only change the relative phase of the two superimposed basis vectors, while their populations remain evenly distributed. The entanglement can also be characterized by the negativity of the partial transpose of the density matrix [6]. For each partial transpose, the negativity is defined as the absolute value of the sum of the negative eigenvalues. The partial transposes corresponding to the two eigenstates are

$$\rho_{n,\pm}^T = \mathcal{N}_{n,\pm}^2 \begin{pmatrix} 0 & 0 & 0 & \sqrt{n}\Omega E_{n,\pm}^* \\ 0 & |E_{n,\pm}|^2 & 0 & 0 \\ 0 & 0 & n\Omega^2 & 0 \\ \sqrt{n}\Omega E_{n,\pm} & 0 & 0 & 0 \end{pmatrix}. \tag{S8}$$

The corresponding negativities are $\sqrt{n}\Omega\,|E_{n,\pm}|\,\mathcal{N}_{n,\pm}^2$, each of which is equal to half of the corresponding concurrence. This implies that there is a monotonous one-to-one correspondence between concurrence and negativity, which ranges from 0 to 1/2.

In our experiment, the eigenstates are extracted from the output state associated with the no-jump trajectory, measured for different interaction times. The system starts from the initial state $|e,0\rangle$. After an interaction time t, the system state, evolved under the NH Hamiltonian, can be expressed as a linear combination of the two eigenstates,

$$|\psi_n(t)\rangle = K_\pm(t)\left(\frac{e^{-iE_{n,+}t}}{\mathcal{N}_{n,+}E_{n,+}}\,|\Phi_{n,+}\rangle - \frac{e^{-iE_{n,-}t}}{\mathcal{N}_{n,-}E_{n,-}}\,|\Phi_{n,-}\rangle\right), \tag{S9}$$

where

$$K_{\pm}(t)=\left(\left|\frac{e^{-iE_{n,+}t}}{\mathcal{N}_{n,+}E_{n,+}}\right|^2+\left|\frac{e^{-iE_{n,-}t}}{\mathcal{N}_{n,-}E_{n,-}}\right|^2\right)^{-1/2}. \tag{S10}$$

Replacing Eq. (2) of the main text into this linear combination of $|\Phi_{n,\pm}\rangle$, we can obtain the state evolution in terms of the basis vectors $|g,n\rangle$ and $|e,n-1\rangle$, given by

$$\begin{aligned}|\psi_n(t)\rangle &= \mathcal{N}_n\{[2\Delta E_n\cos(\Delta E_n t/2)+\kappa\sin(\Delta E_n t/2)]\,|e,n-1\rangle \\ &\quad -i4\sqrt{n}\Omega\sin(\Delta E_n t/2)\,|g,n\rangle\},\end{aligned} \tag{S11}$$

where $\mathcal{N}_n=(|2\Delta E_n\cos(\Delta E_n t/2)+\kappa\sin(\Delta E_n t/2)|^2+|4\sqrt{n}\Omega\sin(\Delta E_n t/2)|^2)^{-1/2}$ is the normalization factor. For the state $|\psi_n(t)\rangle$, the qubit-resonator concurrence is given by

$$\mathcal{E}=\sin(2\theta), \tag{S12}$$

where

$$\theta=\arctan\left|\frac{4\sqrt{n}\Omega\sin(\Delta E_n t/2)}{2\Delta E_n\cos(\Delta E_n t/2)+\kappa\sin(\Delta E_n t/2)}\right|. \tag{S13}$$

S2 . EXPERIMENTAL SETUP AND SYSTEM PARAMETERS

Our device consists of five frequency-tunable superconducting Xmon qubits, labeled as Q_j (j =1 to 5), each with an anharmonicity of approximately $2\pi\times 240$ MHz. Every Xmon qubit has a microwave line (XY line) to drive its state transitions and an individual flux line (Z line) to dynamically tune its frequency. These two constituents consequently make each qubit flexibly on-and-off coupled (with a coupling strength $g_{b,j}$) to a bus resonator R_b with a bare frequency $\omega_b/2\pi\simeq 5.582$ GHz and an energy relaxation time $T_b\simeq 13$ μs. Besides, each qubit is also dispersively coupled to its own readout resonator, whose frequency and leakage rate are denoted by $\omega_{r,j}$ and $\kappa_{f,j}$, respectively. All the readout resonators are coupled to a common transmission line to enable the multiplexed readout of all qubits' states. It is worth pointing out that the readout measurement performed here features both single-shot and quantum nondestructive characteristics, and is achieved with the assistance of an impedance-transformed Josephson parametric amplifier (JPA) with a bandwidth of about 150 MHz. In this experiment, the NH Hamiltonian dynamics is realized by coupling Q_1 to its readout resonator R_1, and Q_2 serves as an ancilla qubit for reading out the joint Q_1-R_1 output state. The parameters of Q_j and R_j ($j=1,2$) are listed in TABLE S1, including energy relaxation time $T_{1,j}$, Ramsey Gaussian dephasing time $T^{\star}_{2,j}$, and spin echo Gaussian dephasing time $T^{SE}_{2,j}$ at their idle frequency $\omega_{id,j}$. The readout fidelity ($F_{k,j}$) is defined as the probability of correctly reading out the state of Q_j when it is in $|k\rangle$. For simplicity, we will omit the subscript "1" of the test qubit and its readout resonator, and use the subscript "a" to denote the ancilla qubit. The detailed experimental setup, including the whole electronics and wiring for the device control, is summarized in Fig. S1. The readout resonator for Q is painted blue as an emphasis in the figure, as it is also used as a decaying resonator for constructing the desired non-Hermitian dynamics.

S3 . CONTROLLED Q-R SIDEBAND COUPLINGS

In a superconducting circuit, the parametric modulation is often achieved by modulating the flux. In our work, the modulation protocol is implemented by applying an external flux of the form

$$\Phi_{ext}(t)=\overline{\Phi}+\tilde{\Phi}\cos(\nu' t), \tag{S14}$$

to tune the transition frequency of the superconducting qubit Q. Here, $\overline{\Phi}$ is the parking flux, $\tilde{\Phi}$ and ν' are, respectively, the modulation amplitude and frequency. The Josephson energy of Q is modified through an external flux Φ_{ext},

$$E_J(t)=E_{J\sum}\left|\cos\left[\pi\frac{\Phi_{ext}(t)}{\Phi_0}\right]\right|, \tag{S15}$$

with $\Phi_0=h/(2e)$ being the flux quantum. Under this modification, the transition frequency of Q is modulated as (setting $\hbar=1$)

$$\omega_e(t)\simeq\sqrt{8E_cE_J(t)}-E_c, \tag{S16}$$

where E_c represents the charge energy. In light of the sinusoidal function in $E_J(t)$ of Eq. (S15), Eq. (S16) can be evaluated by Fourier series expansion, that is,

$$\omega_e(t) = \omega_0 + \sum_{k=1}^{\infty} \varepsilon_k \cos(\omega_k t). \tag{S17}$$

Here, ω_0 stands for the averaged Q transition frequency, and ε_k and ω_k denote the amplitude and frequency of the k-th harmonic, respectively.

Due to the nonlinear flux dependence of $\omega_e(\Phi_{ext})$, the average value ω_0 of the Q transition frequency will be shifted away from $\omega_e(\overline{\Phi})$ by some amount, and this shifted frequency amount can be measured by a Ramsey interferometer. In this experiment, the operation point during the modulation procedure is chosen at the sweet point of Q with $\Phi_{ext} = 0$ and $\overline{\Phi} = 0$. This is because at the Q's sweet point, Eq. (S17) can be substantially simplified to the following compact expression,

$$\omega_e(t) \approx \omega_0 + \varepsilon \cos(\nu t), \tag{S18}$$

by simply keeping one dominant Fourier component while neglecting all the rest higher-order harmonic terms. Here the actual qubit modulation frequency ν is twice that of the corresponding flux modulation [4]. In the experiment, ε can be readily manipulated by tailoring the z-pulse amplitude (zpa).

Under this parametric modulation, the coherent dynamics of the system combined by Q and R is governed by the Hamiltonian (setting $\hbar = 1$)

$$H = \omega_e(t)|e\rangle\langle e| + \omega_r a^\dagger a + g_r(a^\dagger|g\rangle\langle e| + a|e\rangle\langle g|), \tag{S19}$$

where ω_r is the center frequency of the quantized decaying bosonic mode and g_r ascribes the on-resonance coupling strength between Q and R. Now, substituting Eq. (S18) into Eq. (S19) and working in the interaction picture would transform the full Hamiltonian of Eq. (S19) into

$$H_I = g_r e^{i\Delta_r t - i\mu \sin(\nu t)} a^\dagger|g\rangle\langle e| + H.c., \tag{S20}$$

Parameters	Q_1 (Q)	Q_2 (Q_a)
Qubit idle frequency, $\omega_{id,j}/2\pi$	5.99 GHz	5.23 GHz
Coupling strength to the bus resonator R_b, $g_{b,j}/2\pi$	20.9 MHz	20.3 MHz
Coupling strength to the decaying resonator R_j, $g_{r,j}/2\pi$	41 MHz	40 MHz
Energy relaxation time, $T_{1,j}$	14.3 μs	24.8 μs
Ramsey dephasing time, $T^{\star}_{2,j}$	5.3 μs	1.1 μs
Dephasing time with spin echo, $T^{SE}_{2,j}$	14.7 μs	3.5 μs
Frequency of decaying resonator, $\omega_{r,j}/2\pi$	6.66 GHz	6.76 GHz
Leakage rate of decaying resonator, $\kappa_{f,j}$	$1/200\ ns^{-1}$	$1/226\ ns^{-1}$
$\|g\rangle$ state readout fidelity, $F_{g,j}$	0.981	0.977
$\|e\rangle$ state readout fidelity, $F_{e,j}$	0.901	0.902

TABLE S1: **Parameters of the circuit QED system.** The parameters of both the test qubit (Q_1) and ancilla qubit (Q_2) are measured at their idle frequencies $\omega_{id,j}$ ($j = 1, 2$). $\omega_{id,j}$ is also the point at which the single-qubit rotations and state tomographies are performed. $g_{b,j}$ denotes the R_b-Q_j coupling strength, which was inferred from the quantum Rabi signals of Q_j resonantly coupled to R_b. $g_{r,j}$ is the Q_j-R_j coupling strength, which was deducted by measuring the dispersive frequency shift of the decaying resonator. The fidelity for correctly recording each qubit's state in experiment is $F_{k,j}$, characterized by extracting the state information of each readout resonator with the resonance frequency and leakage rate $\omega_{r,j}$ and $\kappa_{f,j}$, respectively.

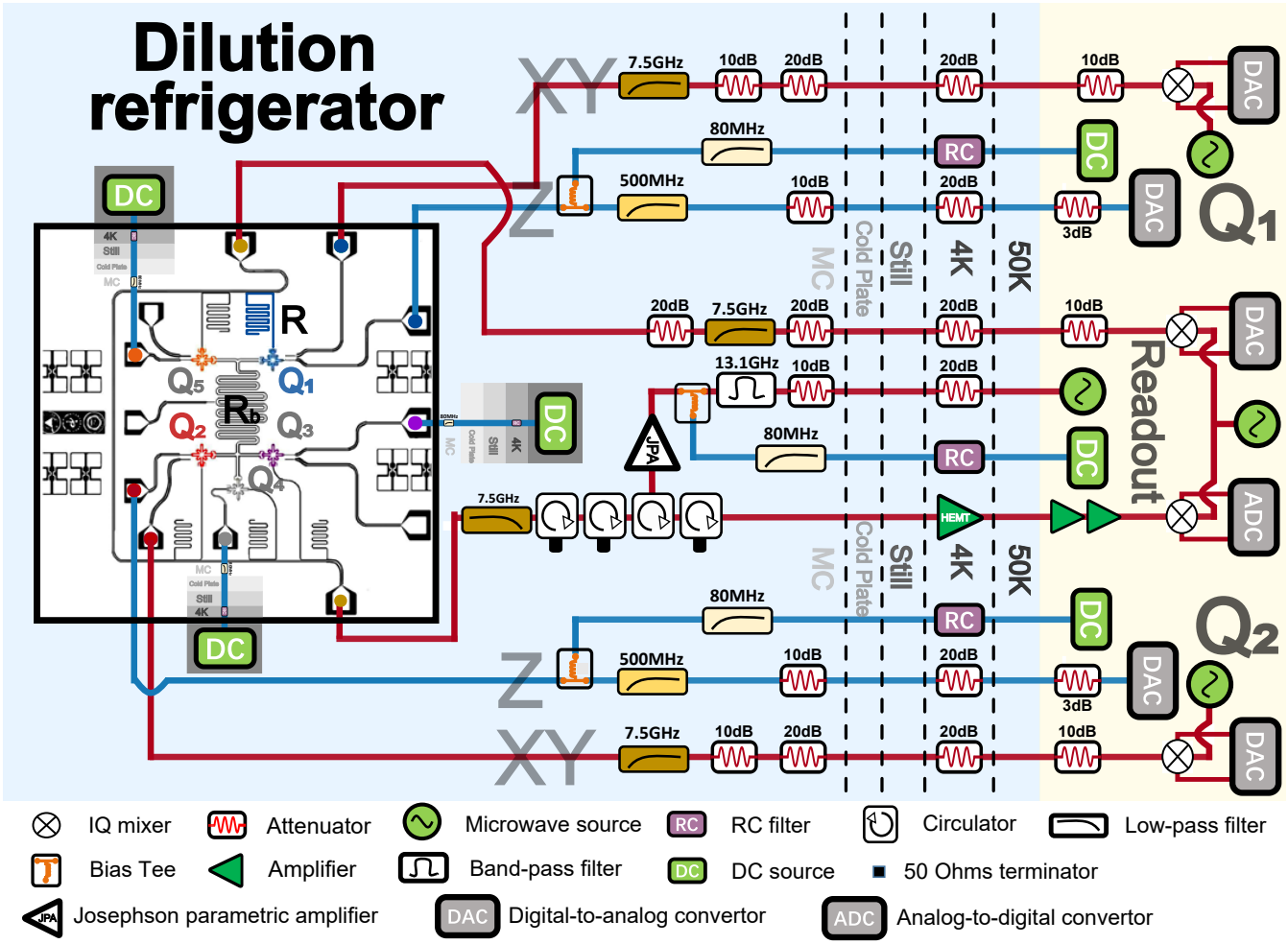

FIG. S1: **Schematic layouts of our circuit QED system and experimental setup.** The superconducting circuit has five frequency-tunable Xmon qubits, labeled from Q_1 to Q_5. Each qubit can be individually frequency-biased and frequency-modulated (through the Z line) and flipped (through the XY line). Thanks to such flexible adjustability, every qubit can be coupled to the bus resonator (R_b) in a controllable way. The XY control of each qubit is implemented by mixing the low-frequency signals (yielded by two Digital-to-analog converter (DAC)'s I/Q channels) with a Microwave source (MS) at 5.5-GHz carrier frequency; while the Z control is fulfilled by two signals: one is produced by the Direct-current (DC) biasing line from a low frequency DC source, and the other is directly obtained from the Z control of a DAC. Meantime, every qubit has its own readout resonator which helps to project out the state information. Experimentally, this is accomplished by the mixing of the signals of two Analog-to-digital converter (ADC)'s I/Q channels and one MS at about 6.6-GHz frequency to output a readout pulse. Both the employed DAC and ADC are field-programmable-gate-array-controlled and respond at the nanosecond scale. The output from the circuit, before being captured and demodulated by the ADC, is sequentially amplified by an impedance-transformed Josephson parametric amplifier (JPA, which is pumped by a 13.5-GHz MS and modulated by a DC bias), a high electron mobility transistor (HEMT), and two room temperature amplifiers. Furthermore, a few custom-made circulators, attenuators, and filters are utilized at some specific locations of the signal lines to reduce the noise that may affect the operations of the device.

where $\mu = \varepsilon/\nu$, $\Delta_r = \omega_r - \omega_0$, and $H.c.$ means the Hermitian conjugate. Using the Jacobi-Anger expansion

$$e^{i\mu \sin\theta} = \sum_{-\infty}^{\infty} J_n(\mu) e^{in\theta}, \tag{S21}$$

with $J_n(x)$ being the n-th Bessel function of the first kind, Eq. (S20) then becomes

$$H_I = g_r \left[\sum_{n=-\infty}^{\infty} J_n(\mu) e^{-i(n\nu - \Delta_r)t} a^\dagger |g\rangle\langle e| + H.c. \right]. \tag{S22}$$

Equation (S22) looks complicated and time-dependent. In practice, its complexity and time-dependence can be easily removed under the conditions $\nu = \Delta_r$ ($\nu = \Delta_r/2$) and $g_r \ll \nu$. Accordingly, this frequency setting is referred to as the first-order (or second-order) sideband modulation for establishing the Q-R coupling with the coupling strength $\Omega = J_1(\mu)g_r$ (or $\Omega = J_2(\mu)g_r$). As a consequence, a swap operation of $|e,0\rangle \leftrightarrow |g,1\rangle$ is available under such a modulation arrangement.

Without considering the interference of R_b, it is favorable to use the second-order sideband coupling due to the limitation of the available modulating flux. However, when this interaction is weak, it may be strongly intervened by the first-order sideband coupling associated with R_b. To optimize the parametric modulation, we prepare Q in the $|e\rangle$-state, and observe the output $|e\rangle$-state population (P_e) after a modulating pulse with a fixed duration of 1 μs. Fig. S2a and Fig. S2b display the populations, measured respectively under the first-order and second-order sideband modulations. Figure S2b shows a crossing region where the qubit Q is effectively coupled to both resonators R and R_b. In this region, the first-order sideband interaction (labeled with "1") with R_b coincides with the second-order sideband interaction (labeled with "2") with R, resulting in undesired effects in our experiments. To circumvent this issue, we use the first-order sideband modulation to realize Q-R swapping interaction for the corresponding region. To confirm the validity of these modulations, in Fig. S2c we present the vacuum Rabi oscillation signals for the test qubit induced by these sideband couplings for different modulating amplitudes. In this way, we arrange our modulation protocol and confine the system's energy-level structure to the configuration shown in Fig. 1 of the main text.

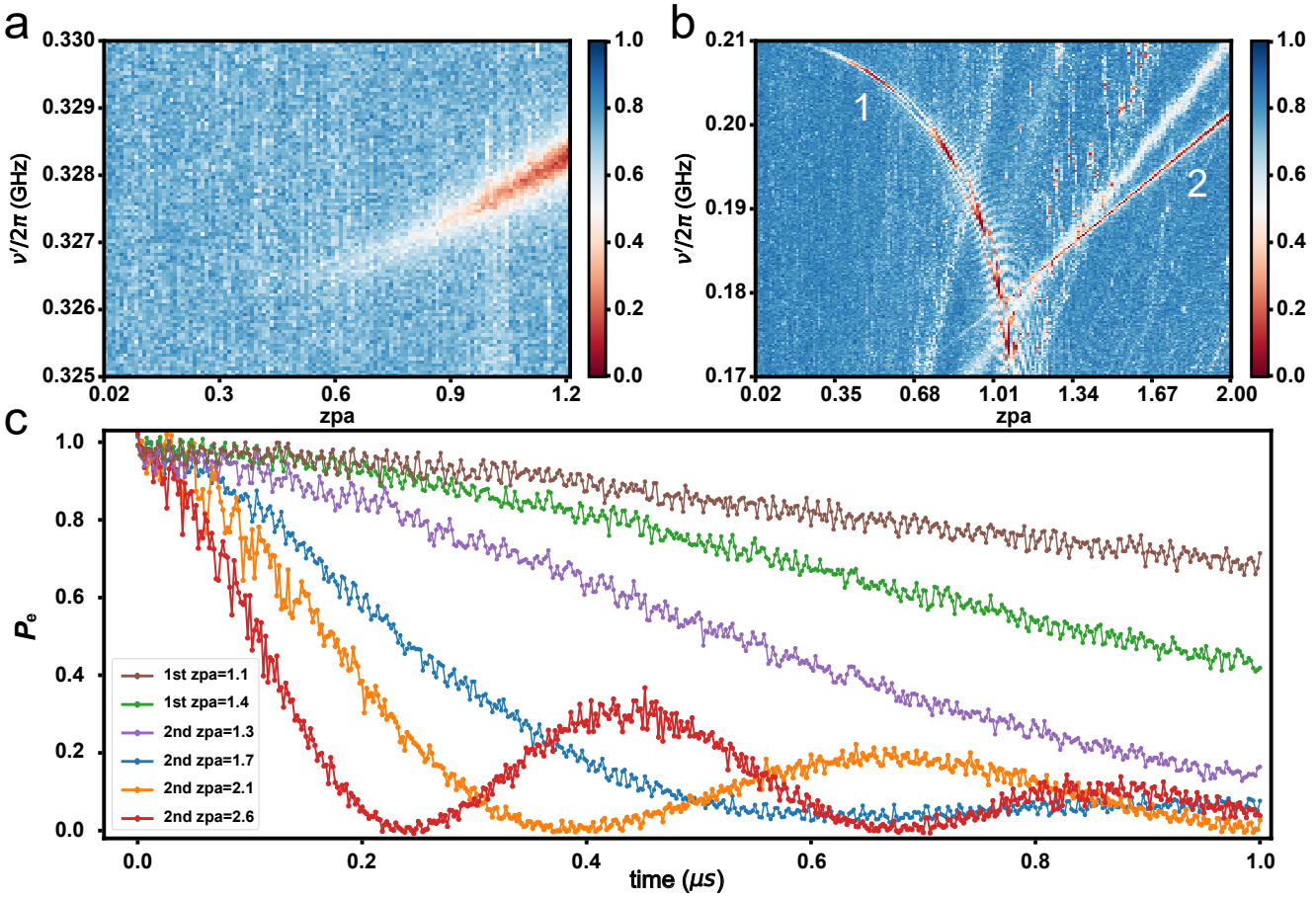

FIG. S2: **Scanning map of the population P_e of the superconducting qubit Q after 1-μs parametric modulations.** (a) The measured data obtained by coupling Q with R via the first-order sideband modulation. (b) The measured data labeled as "1" ("2") attained by establishing the Q-R_b (Q-R) interaction via the first-order (second-order) sideband modulation. Here, the x-axis states the modulation amplitude in zpa and the y-axis gives the modulation frequency. (c) Temporal evolution of the population P_e under different single-tone modulations.

S4 . NUMERICAL SIMULATIONS OF THE NON-HERMITIAN HAMILTONIAN DYNAMICS

To validate the authenticity of the effective NH Hamiltonian presented in Eq. (1) of the main text, we conducted a numerical simulation focusing on the system dynamics associated with the no-jump trajectory, which is governed by the original NH Hamiltonian. This NH Hamiltonian integrates the original coherent Hamiltonian from Eq. (S20) with the NH terms, namely the last two terms of Eq. (1) in the main text. Figures S3a to f illustrate the evolution of the population $|e,0\rangle$ and the qubit-resonator concurrence corresponding to the no-jump trajectory, determined by the original NH Hamiltonian. These results are juxtaposed with those obtained using the effective NH Hamiltonian from Eq. (1) in the main text. The comparative analysis confirms a robust correspondence between the dynamics predicted by the effective NH Hamiltonian and those governed by the original NH Hamiltonian. In addition to the doubled oscillation frequency, the entanglement is much more sensitive to the control parameter. For instance, when the population of state $|g,1\rangle$ changes from 0 to 0.1, the concurrence increases by an amount ~ 0.6, which is one order of magnitude larger than the variation in the population of state $|g,1\rangle$. Therefore, the concurrence (Figs. S3e and f) is much more influenced by the high-frequency oscillating terms than the population (Fig. S3b and c). In these figures, the orange and blue lines respectively denote the numerical results with the effective and full Hamiltonians, and the circles are the experimental data.

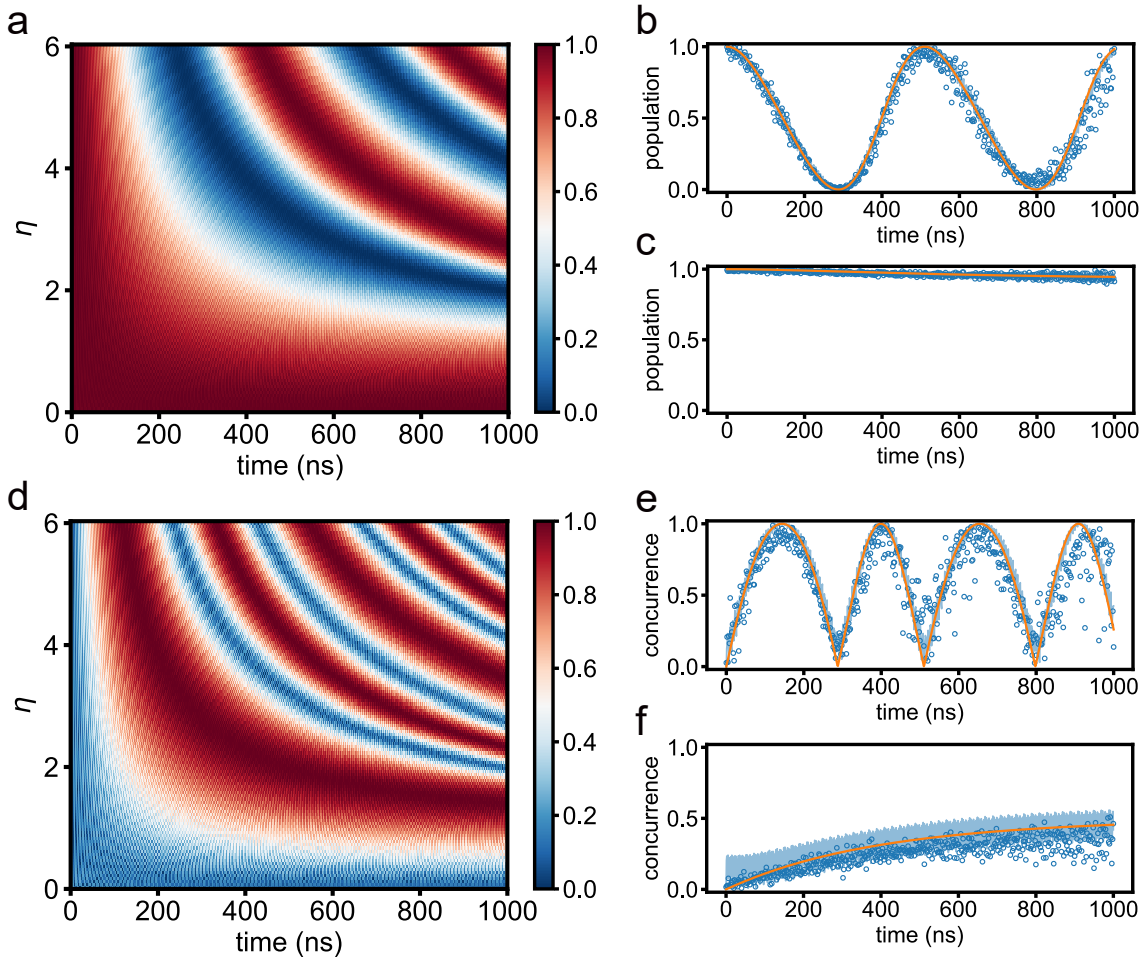

FIG. S3: **Numerical evolutions of the system's non-Hermitian evolution using the full Hamiltonian H_I.** (a) Vacuum Rabi oscillations by calculating $P^N_{|e,0\rangle}$ in terms of the rescaled coupling $\eta = 4\Omega/\kappa$. As an example, (b) and (c) compare $P^N_{|e,0\rangle}$ obtained respectively with use of the full (blue) and effective (orange) Hamiltonians before ($\eta = 5$) and after ($\eta = 0.5$) the exceptional entanglement transition. (d) Concurrence $\mathcal{E}$ evolution for different η. As an example, (e) and (f) compare $\mathcal{E}$ obtained respectively with use of the full (blue) and effective (orange) Hamiltonians before ($\eta = 5$) and after ($\eta = 0.5$) the exceptional entanglement transition. The blue empty circles are experimental data.

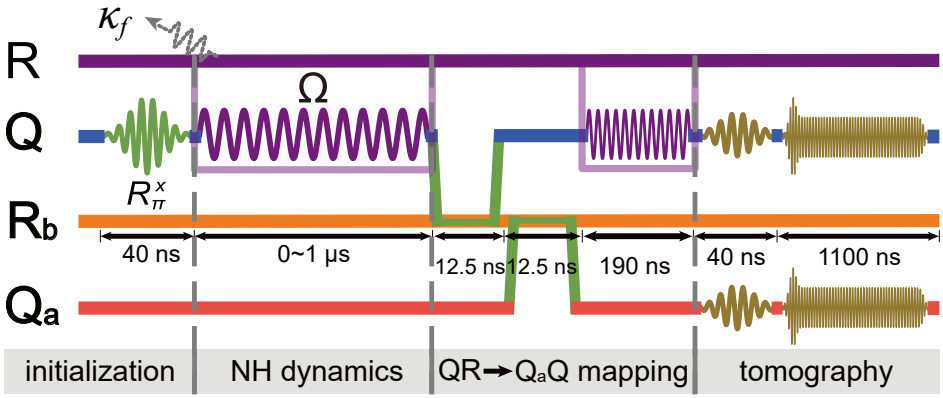

FIG. S4: **Pulse sequence.** The NH dynamics starts with the initial state $|e,0\rangle$, prepared from $|g,0\rangle$ with a π pulse. After a preset evolution time, the parametric modulation is switched off, followed by the state mappings $Q \to R_b$, $R_b \to Q_a$, and $R \to Q$, each realized by an on-resonance swapping gate, where Q_a is an ancilla qubit, and R_b represents the bus resonator coupled to both qubits. After these mappings, the Q-R output state produced by the NH dynamics is encoded in the joint Q_a-Q state, which is then measured by quantum state tomography.

S5 . JOINT Q-R QUANTUM STATE TOMOGRAPHY

The joint Q-R output state after the NH dynamics is read out by mapping it to the Q_a-Q system. The pulse sequence is displayed in Fig. S4. To accomplish this mapping, we must first transfer the state of Q to R_b. This is realized by tuning Q on resonance with R_b for a duration $t = \pi/(2g_b) = 12.5$ ns. After the $Q \to R_b$ state transfer, we reset Q to its idle frequency and bring Q_a resonance with R_b. Similarly, after an interaction duration t, Q_a carries the bus resonator's state. Up to this moment, we complete the state transfer from Q to Q_a.

The next step is to transfer the R-state to Q. Because the R-frequency is much higher than the Q's, it is impossible to realize a quantum state transfer within the same short time period using the resonant coupling technique introduced above. As such, we consider the second-order sideband resonant coupling proposed in Section S3 instead. Limited by the experimental constraints, the maximum achievable coupling strength is about $\Omega_{max} = 2\pi \times 1.18$ MHz, which gives rise to the fastest state transfer time duration of approximately $\tau = 193$ ns. This period is comparable to the lifetime of the readout resonator so that the dissipation of R has a significant impact on the state mapping.

However, there is a one-to-one correspondence between the Q_aQ output state after the state mapping and Q-R state just before the mapping for the no-jump case, as interpreted below. Without loss of the generality, the Q-R state right before the state mapping can be expressed as

$$|\psi_0\rangle = c_1|e,0\rangle + c_2|g,1\rangle, \tag{S23}$$

with $|c_1|^2 + |c_2|^2 = 1$. After the state mapping, the Q_a-Q output state is

$$|\psi_1\rangle = (1/\sqrt{|c_1|^2 + k^2|c_2|^2})(c_1|e_a,g\rangle + kc_2|g_a,e\rangle), \tag{S24}$$

where $k = e^{-\kappa_f t}e^{-\kappa_f \tau/4}$. For simplicity, we here do not include the phase accumulated during the mapping. This implies that the original Q-R output state $|\psi_0\rangle$ can be inferred from $|\psi_1\rangle$ by multiplying the coefficient of the component $|g_a,e\rangle$ by $1/k$ and then renormalizing the resulting state. In the experiment, the Q_a-Q output state is characterized by the two-qubit density matrix, which is reconstructed through joint quantum state tomography. The result associated with the no-jump trajectory is obtained by projecting the density matrix to the single-excitation subspace $\{|e_a,g\rangle, |g_a,e\rangle\}$, which can be expressed as

$$\rho_1 = \begin{pmatrix} \rho_{11} & \rho_{12} \\ \rho_{21} & \rho_{22} \end{pmatrix} \tag{S25}$$

The elements of Q-R density matrix within $\{|e,0\rangle, |g,1\rangle\}$ right before the state mapping are related to those of ρ_1 by

$$\rho_1 = \frac{1}{\rho_{11} + \rho_{22}/k^2} \begin{pmatrix} \rho_{11} & \rho_{12}/k \\ \rho_{21}/k & \rho_{22}/k^2 \end{pmatrix} \tag{S26}$$

S6 . QUBIT READOUT CORRECTIONS

The fidelity matrix for calibrating the measured probabilities is defined as

$$\hat{F} = \begin{pmatrix} F_g & e_{ge} \\ e_{eg} & F_e \end{pmatrix}, \tag{S27}$$

where F_j $(j = g, e)$ represents the probability for correctly reading out the state of the qubit when it is in $|k\rangle$, and e_{jk} $(j, k = g, e)$ stands for the error that describes the leakage probability from the state $|k\rangle$ to state $|j\rangle$. To illustrate how the qubit readout error can be corrected, we denote the measured probability distribution as $\hat{P}_M$ and the genuine probability distribution as $\hat{P}_N$. The relation among $\hat{F}$, $\hat{P}_M$, and $\hat{P}_N$ is established by the following simple identity,

$$\hat{P}_M = \hat{F} \cdot \hat{P}_N. \tag{S28}$$

The above relation (S28) implies that the genuine states of the system can be mathematically reconstructed by performing the matrix inversion of $\hat{F}$, i.e., $\hat{P}_N = \hat{F}^{-1} \cdot \hat{P}_M$. The data used in our calibrations are extracted from the measured I-Q (in phase and quadrature) values, as shown in Fig. S5. According to the measured data, in this work

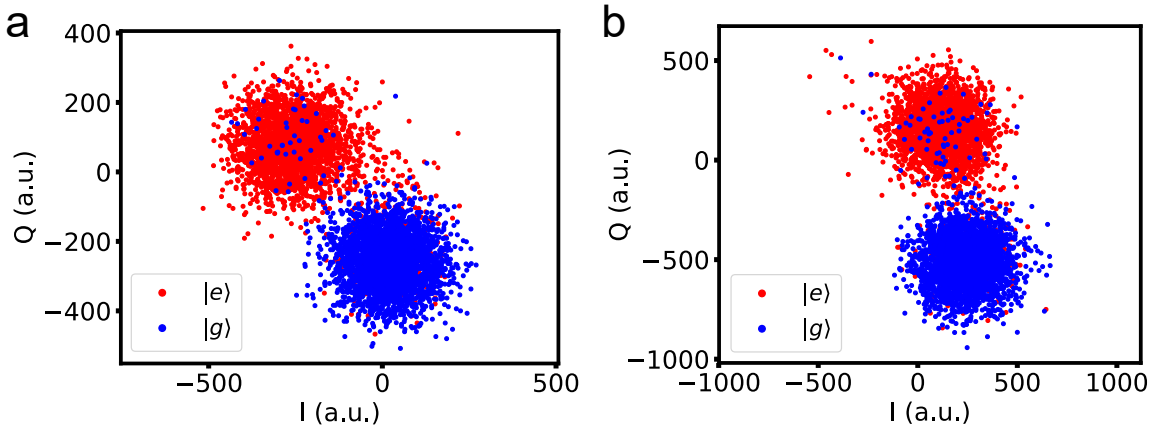

FIG. S5: **Qubit readouts for Q (a)** and Q_a **(b)** with 3000 repetitions and 1.1-μs readout duration.

the fidelity matrices for Q and Q_a are

$$\hat{F}_Q \simeq \begin{pmatrix} 0.981 & 0.099 \\ 0.019 & 0.901 \end{pmatrix}, \quad \hat{F}_{Q_a} \simeq \begin{pmatrix} 0.977 & 0.098 \\ 0.023 & 0.902 \end{pmatrix}. \tag{S29}$$

In the computational basis, the joint QST measurement on Q and Q_a can be therefore corrected by the following formula,

$$\hat{P}_N = (\hat{F}_Q \otimes \hat{F}_{Q_a})^{-1} \cdot \hat{P}_M. \tag{S30}$$

S7 . EXTRACTION OF EIGENENERGIES AND EIGENSTATES OF THE NON-HERMITIAN HAMILTONIAN

After collecting the data, we have applied the least-squares fitting to the measured density matrix ρ in order to extract the eigenenergies and eigenstates of the system. Theoretically, for a certain point in the parameter space, we can in principle write the eigenenergies and the corresponding eigenstates of the non-Hermitian system as

$$E_\pm = c_{\pm,1} + i c_{\pm,2}, \quad |\Phi_\pm\rangle = \alpha_\pm |g, 1\rangle + \beta_\pm |e, 0\rangle, \tag{S31}$$

where $c_{\pm,1}$, $c_{\pm,2}$, $\alpha_\pm$ and $\beta_\pm$ are the fitting parameters. If we assume the system's initial state to be

$$|e, 0\rangle = \frac{1}{\alpha_-\beta_+ - \alpha_+\beta_-}(\alpha_- |\Phi_+\rangle - \alpha_+ |\Phi_-\rangle), \tag{S32}$$

then at time t the system will evolve into the following state

$$|\psi(t)\rangle = \frac{1}{\alpha_-\beta_+ - \alpha_+\beta_-}(\alpha_- e^{-iE_+t}|\Phi_+\rangle + \alpha_+ e^{-iE_-t}|\Phi_-\rangle). \tag{S33}$$

To minimize the fitting errors, we have defined an error function as a guidance, which has the form of

$$\text{erf} = \text{Tr}[\rho|\psi(t)\rangle\langle\psi(t)|] - 1. \tag{S34}$$

Based on this error function, the next step is to seek the fitting parameters which can minimize Eq. (S34) at each moment. In this way, a reliable least-squares fitting to the entire evolution of the density matrix ρ is found with all the parameters: $c_{\pm,1}$, $c_{\pm,2}$, $\alpha_\pm$, $\beta_\pm$.

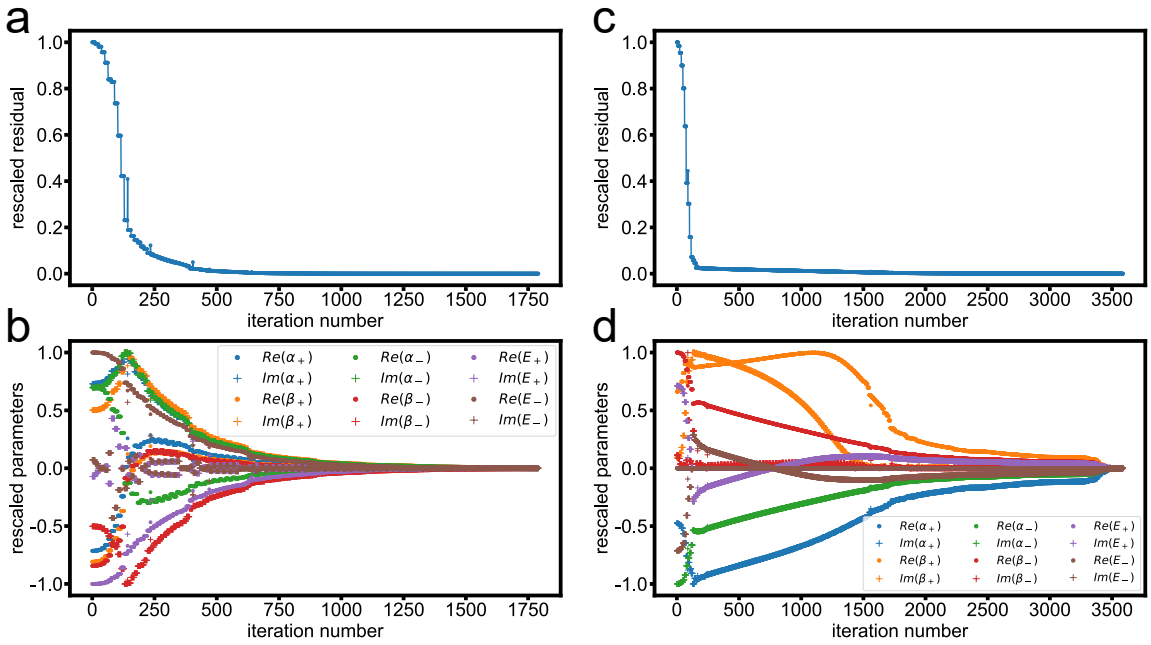

FIG. S6: **Convergence of residuals and parameters.** (a) (b) Above the EP, $\eta = 5$. (c) (d) Below the EP, $\eta = 0.5$.

The convergence condition is critical for ensuring the success of a fitting process. In Fig. S6, we show the convergence of residuals and all parameters as functions of the number of iterations. To facilitate comparison, we rescaled each parameter to an appropriate size, using $[f_i - f_N]/[max(f) - min(f)]$, where f represents the set of results after each iteration, f_i represents the result of the i-th iterations, and $i = 0, 1, 2, ..., N$, with N being the maximum iteration number. We observe that all parameters converge together after a sufficient number of iterations. We provide two representative examples, one for $\eta = 5$ (above the EP, shown in Figs. S6a and b) and the other for $\eta = 0.5$ (below the EP, shown in Figs. S6c and d). We verified the validity of the remaining fitting procedures using the same approach.

We also calculate the fidelities of the eigenstates ($|\Phi'_\pm\rangle$) obtained in this manner with respect to the ideal ones $|\Phi_\pm\rangle$, which are defined as

$$\mathcal{F}_\pm = |\langle\Phi'_\pm|\Phi_\pm\rangle|^2. \tag{S35}$$

The fidelities as functions of η are presented in Figs. S7a and b, respectively. The dip in Fig. S7b is mainly caused by two factors. First, we can observe from the comparison between Figs. S3e and f that the effect of off-resonant terms in the parametric modulation is more significant when $\eta < 1$. This is demonstrated by the oscillations in Fig. S3f having a significantly larger amplitude than those in Fig. S3e. Second, when $\eta < 1$, the system's evolution is likewise more susceptible to dephasing, resulting in an overall measured concurrence (associated with the non-diagonal elements of the density matrix) that is lower than the theoretical value, as illustrated in Fig. S3f. Therefore, the fitting error grows as the observed result deviates more from the theoretical value, leading to lower fidelity. Additionally, we discovered that when A¡1, the fitting results are more sensitive to the initial guess and that adjusting the initial guess appropriately can lead to better fitting results, as shown in Fig. S8. The results demonstrate that the eigenstates, extracted from the measured two-qubit output density matrices by our density-matrix post-projecting method, well

agree with the ideal ones, associated with the no-jump evolution trajectories. This agreement confirms the validity of approximations for deriving the effective NH Hamiltonian, as well as the soundness of the density-matrix post-projecting method.

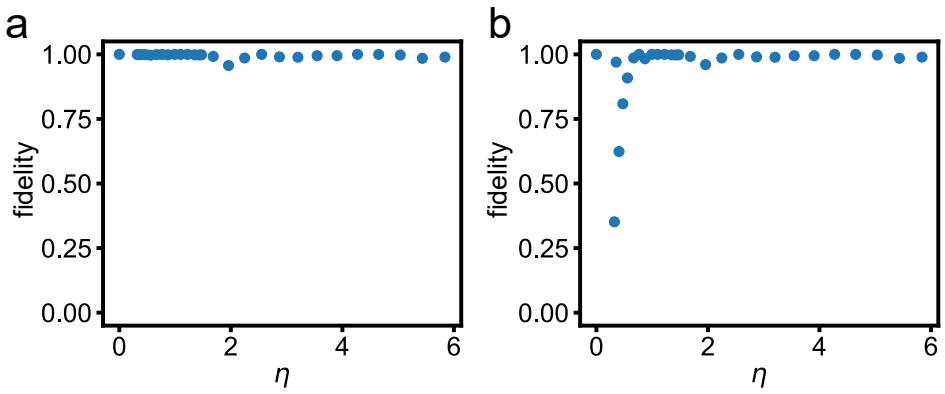

FIG. S7: **Fidelities of fitted eigenstates.** (a) $\mathcal{F}_+$ as as a function of η. (b) $\mathcal{F}_-$ as as a function of η.

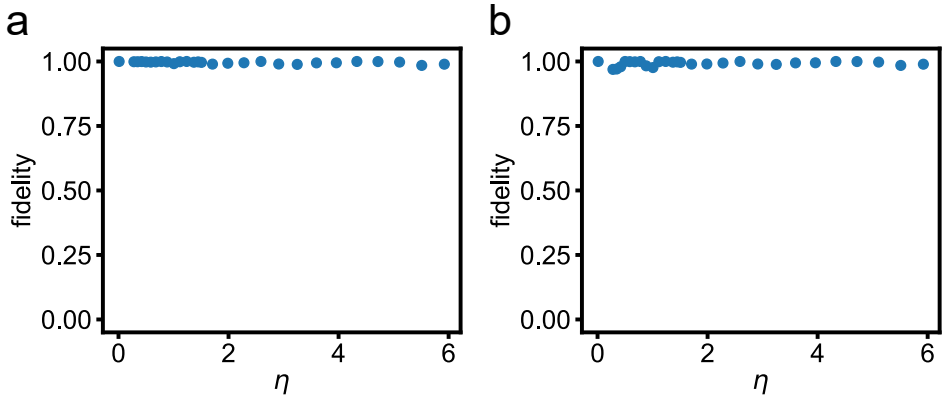

FIG. S8: **Fidelities of fitted eigenstates after adjusting initial guesses.** (a) $\mathcal{F}_+$ as as a function of η. (b) $\mathcal{F}_-$ as as a function of η.

S8 . EXCEPTIONAL ENTANGLEMENT TRANSITION IN A TWO-QUBIT SYSTEM

The exceptional entanglement transition is not restricted to the light-matter system, but is a universal behavior for a variety of NH interacting quantum systems. As a paradigmatic example, we here consider the system composed of two decaying qubits interacting with each other by swapping coupling [1–3]. When the two qubits have the same frequency, the no-jump evolution trajectory is governed by the NH Hamiltonian (setting $\hbar = 1$)

$$\mathcal{H}_{NH} = \Omega(\sigma_1^+\sigma_2^- + \sigma_1^-\sigma_2^+) - \frac{i}{2}(\kappa_1 |e_1\rangle\langle e_1| + \kappa_2 |e_2\rangle\langle e_2|), \tag{S36}$$

where $\sigma_j^+ = |e_j\rangle\langle g_j|$ and $\sigma_j^- = |g_j\rangle\langle e_j|$ with $|e_j\rangle$ ($|g_j\rangle$) denoting the upper (lower) level of the jth qubit, κ_j is the dissipation rate of $|e_j\rangle$, and Ω is coupling strength. This swapping coupling does not change the total excitation number of the system. When the system is initially in a one-excitation state, its dynamics will be restricted within the subspace $\{|e_1, g_2\rangle, |g_1, e_2\rangle\}$. In such a subspace, the eigenstates of the NH Hamiltonian are given by

$$|\Phi_\pm\rangle = \mathcal{N}_\pm(\Omega |e_1, g_2\rangle + \Gamma_\pm |g_1, e_2\rangle), \tag{S37}$$

where $\mathcal{N}_\pm = (\Omega^2 + |\Gamma_\pm|^2)^{-1/2}$ and $\Gamma_\pm = -i\kappa/4 \pm E_g/2$ with $\kappa = \kappa_2 - \kappa_1$. The energy gap between these two eigenstates is $E_g = 2\sqrt{\Omega^2 - \kappa^2/16}$.

When the two qubits have distinct decaying rates, these eigenstates and eigenenergies have the same forms as those of the qubit-resonator system. Consequently, the energy gap undergoes a real-to-imaginary transition at the EP $\eta = 4\Omega/|\kappa| = 1$, which is accompanied by an entanglement transition of the eigenstates. The two-qubit concurrences [5] for the two eigenstates $|\Phi_\pm\rangle$ are

$$\mathcal{E}_\pm = \frac{2\Omega\,|\Gamma_\pm|}{|\Gamma_\pm|^2 + \Omega^2}. \tag{S38}$$

When $\eta \to 0$, the two eigenstates respectively reduce to $|e_1, g_2\rangle$ and $|g_1, e_2\rangle$, each of which has no entanglement. When $\kappa_2 \ll \kappa_1$, the concurrence is increased linearly with η until reaching the EP, where the energy gap vanishes and both eigenstates approximately converge to the same maximally entangled state

$$|\Phi_\pm\rangle = (|e_1, g_2\rangle - i\,|g_1, e_2\rangle)/\sqrt{2}. \tag{S39}$$

After crossing the EP, $|\Phi_\pm\rangle$ move in opposite directions, but with the concurrences $\mathcal{E}_\pm$ remaining to be 1, independent of η.

---

[1] S.-B. Zheng and G.-C. Guo, Efficient scheme for two-atom entanglement and quantum information processing in cavity QED, *Phys. Rev. Lett.* **85,** 2392-2395 (2000).

[2] S. Osnaghi, P. Bertet, A. Auffeves, P. Maioli, M. Brune, J. M. Raimond, and S. Haroche, Coherent control of an atomic collision in a cavity, *Phys. Rev. Lett.* **87,** 037902 (2001).

[3] C. Song *et al.*, 10-qubit entanglement and parallel logic operations with a superconducting circuit, *Phys. Rev. Lett.* **119,** 180511 (2017).

[4] Y. Zhou *et al.*, Rapid and unconditional parametric reset protocol for tunable superconducting qubits, *Nat. Commun.* **12,** 5924 (2021).

[5] W. K. Wootters, Entanglement of formation of an arbitrary state of two qubits, *Phys. Rev. Lett.* **80,** 2245-2248 (1998).

[6] R. Horodecki, P.Horodecki, M.Horodecki, and K. Horodecki, Quantum entanglement, *Rev. Mod. Phys.* **81,** 865 (2009).